Wake identification of stratified flows using dynamic mode decomposition

Chan-Ye Ohh and Geoffrey R. Spedding

Phys. Rev. Fluids **7**, 024801 — Published 22 February 2022

DOI: 10.1103/PhysRevFluids.7.024801

Wake identification of stratified flows using Dynamic Mode Decomposition

Chan-Ye Ohh and Geoffrey R. Spedding
Department of Aerospace and Mechanical Engineering,
University of Southern California, Los Angeles, CA 90089-1191
(Dated: January 13, 2022)

ABSTRACT. The wake behind a bluff body in the presence of a density gradient is characterized by competing effects of buoyancy, momentum and ultimately viscosity as the flow decays. Consequently, there are a number of distinct flow regimes into which the wakes can be placed, and there is some interest in whether any given wake can be traced back to its source through interrogation of selected fluid mechanical properties in the wake. Here we use Dynamic Mode Decomposition (DMD) to find modes that can be used to characterize and automate such a process. A custom-designed algorithm is proposed that can sort and classify stratified wakes based on a selection of the most energetic DMD modes. The approach is very, or partially successful, depending on the quality and dimension of the input data. The success of these first steps may be used to develop similar methods for more challenging and fully turbulent wakes, and also can serve as a guide for data-driven methods that require no prior knowledge of the flow structure.

I. INTRODUCTION

A. Sphere wakes in a stratified fluid

Significant parts of the earth's atmosphere and ocean have gradients in pressure and temperature (troposphere) or temperature and salinity (thermocline) that result in stable and persistent gradients in density with height. In the ocean thermocline, the upper 500 m (apart from a thin surface wind-induced mixed layer) can be modeled with a constant, linear density gradient $d\rho/dz$. This density gradient is stable so that perturbations give rise to restoring wave motions with a natural frequency $N = [(-g/\rho_0) \cdot (d\rho/dz)]^{1/2}$, where ρ_0 is a mean density and g is the gravitational acceleration. For a body of size D moving at speed U through this thermocline, the ratio of buoyancy timescales to convective timescales is expressed by the internal Froude number, $Fr = 2U/ND$, and when coupled with the usual Reynolds number, $\mathrm{Re} = UD/\nu$, where ν is the kinematic viscosity, the {Re-Fr} space is characterised by a wide range of internal wave and vortex shedding modes and interactions, especially at moderate values of both, $\mathrm{Re} \in [100, 1000]$ and $\mathrm{Fr} \in [0.1, 10]$.

The {Re-Fr} parameter space was mapped out and described quite comprehensively in experiments by [1](LI92) and [2](CH93). The two sets of classifications are similar, though differing in detail (Fig. 1). Over a range of $10 \leq \mathrm{Re} \leq 10^4$ and $0.02 \leq \mathrm{Fr} \leq 20$. LI92 described 6 principal regimes from steady attached vortices at low {Re-Fr} to fully turbulent wakes at high {Re-Fr}. In general, increases in Re were marked by transitions from steady to unsteady vortex shedding and the development of finer scales as the wake shear layers themselves become unstable. Increases in Fr governed the transitions from laminar uniform wakes without notable vertical excursions, to intermediate stages dominated by strong lee waves as the flow can traverse over and below the sphere, and then to the turbulent state at high Fr.

CH93 described 4 principal regimes over $150 \leq \mathrm{Re} \leq 5 \times 10^4$ and $0.25 \leq \mathrm{Fr} \leq 12.7$, controlled mainly by Fr. At low $\mathrm{Fr} \in [0.25, 0.8]$ the wake has two separate lee wave layers separated by a quasi-two-dimensional region where the flow passes horizontally around the sphere. As Fr increases from 0.25 to 0.8 there are flow states with attached, oscillating, and then steady vortices as the structure becomes increasingly influenced by the strong lee waves. When $\mathrm{Fr} \approx 1$ the buoyancy and convective timescales are approximately equal and CH93 termed this the saturated lee wave regime. As Fr increases from 1.5 to 4.5 a transitional regime marks a gradually decreasing influence of stratification close to the sphere, and there are differences depending on Re just as there are in a homogeneous fluid. For $\mathrm{Fr} > 4.5$ the near wake has 2 modes, a spiral instability mode and Kelvin-Helmholtz modes associated with the wake shear layers. LI92 covered more details at low {Re-Fr}, and CH93 had more at higher values of both parameters. Though there are differences between them, the overall regime diagram for structures and patterns that can emerge into the near wake are quite consistent.

Early direct numerical simulations (DNS) [3] were confined to lower $\mathrm{Re} = 200$ for $0.25 \leq \mathrm{Fr} \leq 200$ but the determining influence of the lee waves was noted, just as found in the subsequent experiments. Body-inclusive simulations were also run by [4] at $\mathrm{Re} = 200$, $\mathrm{Fr} \in [0.1, 0.4]$ (for comparison with [3]) and at $\mathrm{Re} = 1000$ for $\mathrm{Fr} \in [1.0, 16]$ so as to include the commencement of small-scale and turbulent motions on wake measures of fluctuating quantities. At $\mathrm{Re} = 200$, a transition Fr between 0,4 and 0.5 was observed where vortex shedding re-emerges at the lower Fr. Significant differences with [3] were found when $\mathrm{Fr} < 0.5$, and though numerical resolution could be a limiting factor when $\mathrm{Fr} < 0.2$, the discrepancy in computed C_D was not resolved.

DNS by [5] for $\mathrm{Re} = 3700$ and $\mathrm{Fr} \in [0.025, 1]$ showed not only that vortex shedding re-appears at $\mathrm{Fr} < 0.5$ but also that in the combination when Re is sufficiently high

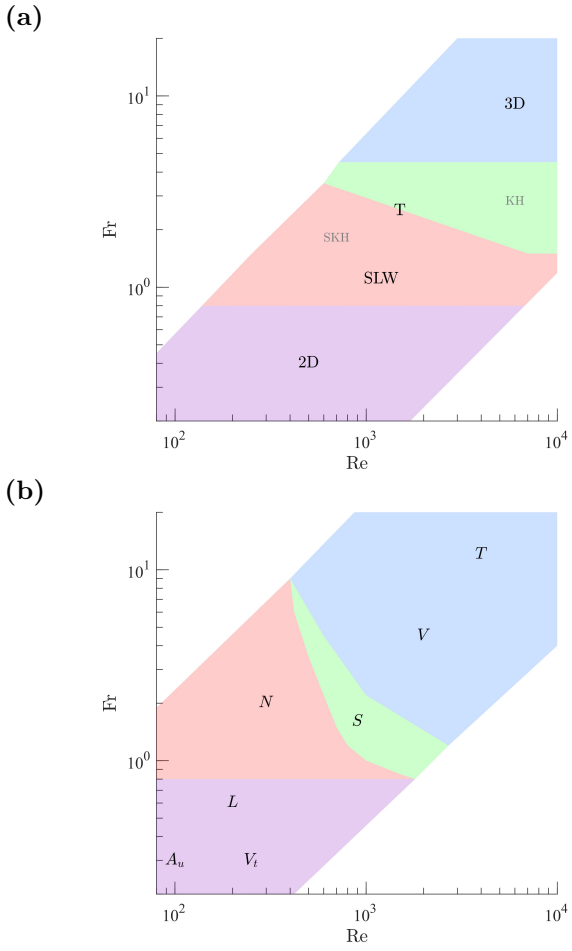

FIG. 1: Regime diagrams from CH93 (a) and LI92 (b). The 4 main regimes differentiated in (a) are: 2D, quasi-2D; SLW, strong lee wave; T, transition (SKH, without K-H instability; KH, with K-H instability); and 3D, three-dimensional. In (b), LI92 distinguished 6 main regimes: A_u, unsteady, attached 2D vortices; V_t, 2D vortex shedding; L, lee-wave instability; N, non-axisymmetric attached vortex; S, symmetric vortex shedding; V, non-symmetric vortex shedding; and T, turbulent wake.

and Fr ≤ 0.125, small-scale fluctuations re-emerge due to wake flapping and secondary turbulence from Kelvin-Helmholtz instability of strongly sheared, strongly stratified layers. These phenomena were further elaborated by [6] who associated the near wake fluctuations with high vortex stretching rates due to the unsteady separating boundary layer at low Fr. A further study [7] at Re $= 3700$, Fr $= [1, 2, 3]$ focused on the role of lee waves at moderate Fr in contributing to the particular wake dynamics in stratified flows.

B. Universal late wakes?

The wakes described above in numerical and laboratory experiments are qualitatively different as competing effects of stratification and increasing Reynolds number generate different dynamical balances that then evolve downstream. However, profiles of mean and fluctuating late wake quantities [8, 9] were shown to be self-similar, and could be rescaled according to U and D without reference to Fr, as if in the far wake, the initial Fr had no influence. Moreover, a simple modification to this scaling, taking into account the magnitude of the initial streamwise momentum flux, showed that the wakes of bluff, streamlined and sharp-edged bodies could all be described by the same power law functions. Given U, D and a drag coefficient (that depends on the streamwise momentum flux, and hence does depend on the shape), the horizontal and vertical growth rates and the decay of mean and fluctuating velocities were all the same [10]. Meanwhile, numerical simulations of stratified wakes that were initialised with prescribed mean and turbulence profiles appeared to evolve in much the same way [11–15], supporting the idea that local turbulence, or post-turbulence dynamics primarily govern the flow, regardless of details of initial conditions.

This lack of sensitivity to initial conditions may be surprising given the very different near-wake regimes detailed in the experiment. It could be that universality is only achieved when values of the governing parameters Re and Fr are high enough, and the observed collapse of experimental data [8] occurred only when Re $\geq 4 \times 10^3$ and Fr ≥ 4. Perhaps only when turbulence over a range of scales is allowed can the cascades in energy and enstrophy proceed along common trajectories. These kinds of arguments have been made in some detail [16–18] where a buoyancy Reynolds number that depends on both Re and Fr, $\mathrm{Re}_b = \mathrm{ReFr}^2$, is used as a diagnostic for the stratified flow dynamics. (There are details of the particular choice of length and velocity scales that matter, but they need not be elaborated at this level.) There is also evidence from both experiments [19–21] and simulations [22] that the scale similarity proposed [23] for homogeneous wakes and turbulent free-shear flows may not happen.

Finally, just because the information from initial conditions is not clearly measured in average wake statistics does not mean that information from the wake-creator is entirely absent, only that it does not affect certain statistical properties. The possibility of pattern detection, and the information that such a pattern could contain remain of interest [24]. One place to start looking is to find and characterize wake pattern information that then might persist downstream, when we will then know what to look for.

C. Coherent structure identification method

Identifying patterns in stratified flows can benefit from data-driven modal decomposition by representing the nonlinear and high-dimensional nature of fluid flows in a low-order model. Many modal decomposition methods such as POD (Proper Orthogonal Decomposition) [25] and DMD (Dynamic Mode Decomposition) [26] have been used to identify physically-relevant coherent structures. While POD provides orthogonal modes that are spatially coherent, DMD computes modes that grow and decay from a temporal orthogonalization, which represents the dynamical importance [27, 28]. DMD modes are equivalent to DFT (Discrete Fourier Transform) modes in a periodic flow or a mean-subtracted DMD, despite having an unrelated derivation [28, 29]. Therefore, DMD is especially useful to identify temporally evolving patterns in stratified flows where the effect of the stratification is time-dependent.

D. Objectives

This work aims to test a pattern classification procedure that is based on DMD modes of stratified wakes at moderate {Re-Fr} where there are distinct, identifiable regimes, all ultimately based on the balance between momentum and buoyancy (Fr) and inertia and viscosity (Re). To do this, we will first propose a combined and simplified wake regime classification that reconciles the existing literature (LI92, CH93), and selects for information that could, in principle, appear in the later wake (so details of separation patterns on the body surface, for example, are ignored). An automated classification is then attempted on the wake data alone. The tests are conducted on the DMD modes because they contain information based on the flow dynamics and sorting or ranking of these modes can extract the most important physical characteristics. The procedure is tested on 3D data from numerical simulations and 2D data from laboratory experiments. Anticipating that future applications will not be on complete datasets, preliminary tests on reduced data are described, and serve to indicate whether the effort could be extended to regimes of significantly higher Re and Fr.

II. METHODS

To study the wake characteristics of each regime that is identifiable by a wake classifier, both computational and laboratory experiments were conducted in the same {Re-Fr} parameter space: $\mathrm{Re} = UD/\nu = [200, 300, 500, 1000]$ and $\mathrm{Fr} = U/(NR) = [0.5, 1, 2, 4, 8, 16]$. The simulation is in the sphere reference frame while the experiment is in a fixed laboratory frame with a moving sphere. The reference frame of the experiment was changed from a towed sphere to a fixed sphere frame to compare the performance of the wake classifier on an equivalent basis.

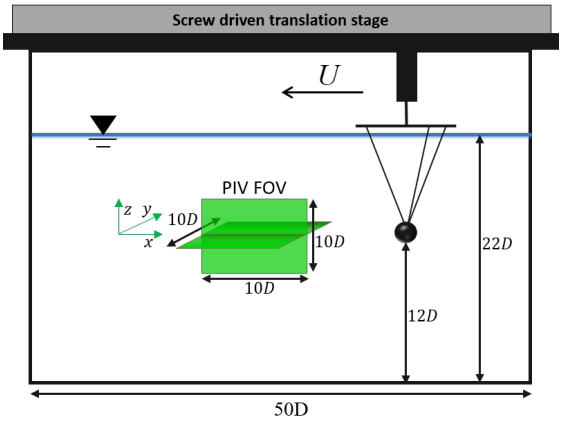

FIG. 2: Schematic showing experimental setup. The annotated scale is based on a sphere with $D = 4$cm to provide a relative scale of the experiment.

A. Experiments

A sphere was towed horizontally in a tank of 1 x 1 x 2.5 m, filled with stably stratified fluid as illustrated in Fig. 2. Refractive index matched salt-stratified water with a linear density gradient was achieved by implementing the RIM technique from Xiang *et al.*[30] to reduce optical distortions. The sphere was submerged to a depth of 0.51 m and attached to the translation stage by three fishing wires. The sphere shells were 3D-printed using polylactic acid (PLA) and filled with a steel ball and clay for stability. The buoyancy frequency $N = [0.13 - 1.0]$ rad/s, sphere radius $R = [0.72 - 5.5]$ cm and tow speed $U = [0.37 - 43]$ cm/s were adjusted to obtain the targeted Fr and Re.

The flowfield was estimated using a LaVision PIV (Particle Image Velocimetry) system with multiple cameras (LaVision-Imager sCMOS), each having a resolution of 2560 × 2160 pixels. Two camera configurations were used for varying Re. In the planar configuration, usually used for lower Fr, Re, the cameras were aligned side-by-side and perpendicular to the center plane with $\sim 5\%$ overlap to obtain an extended field of view (FOV) in the streamwise direction. The FOV of each camera was approximately 35 mm x 300 mm, which is $[x/R, y/R] = [6.5 - 49, 5.5 - 42]$ for the vertical plane and 230 mm x 190 mm, which is $[x/R, y/R] = [4.2 - 32, 3.5 - 26]$ for the horizontal plane. The measurement plane was illuminated with a pulsed laser (Nd:YAG, LaVision NANO L100-50PIV) in either the vertical XOZ center plane or horizontal XOY center plane with a 2 mm thickness sheet. The sphere entered the FOV 70 cm from the starting point, which is $[12.7 - 97.2]R$ (depending on the sphere size), to reduce startup effects. The laser repetition rate

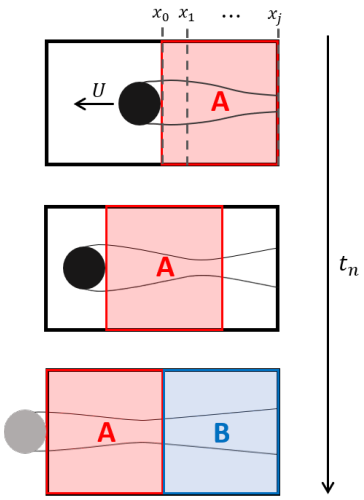

FIG. 3: Temporal data reconfiguration where the colored box A is moving in reference to the sphere. Dashlines indicate column vectors of velocity field within the box A

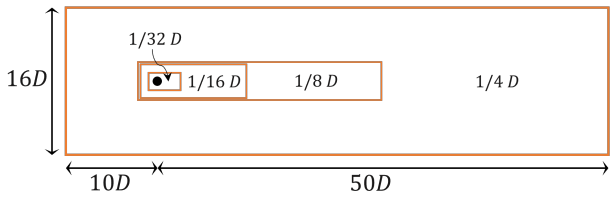

(a) Mesh for Re $= [200, 300, 500]$ has four refinement levels: $2^{-[2\cdots5]}D$

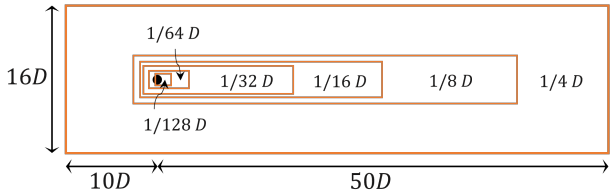

(b) Mesh for Re $= 1000$ has six refinement levels: $2^{-[2\cdots7]}D$

FIG. 4: Meshing in simulation and the location of refinement levels. The computational domain is $(x, y, z) = ([-10, 50], [-8, 8], [-8, 8])D$ and the results in $([1.5, 15], [-2, 2], [-2, 2])D$ was used.

was 5-20 Hz, scaled on the towing velocity. The fluid was seeded with titanium dioxide particles with an average density $4.23g/\text{cm}^3$ and diameter 15μm. Based on Stokes' law, the sink speed is approximately $v_{\text{TiO}_2} = 0.43$mm/s, which gives 7.8-10 min for particles to cross the sphere. The average particle image density was 0.04/pixel.

1. *Temporal reconfiguration of the experimental data*

For the reference frame to be consistent with the simulation, the reference frame of the experimental data was switched to a sphere-fixed frame (a necessary step for temporal DMD). The timescale, Nt, of the wake evolution can be written $Nt = (x/R)/Fr$. Here Nt and x/R will be used interchangeably to denote downstream distance. As illustrated in Fig. 3, a fixed sphere frame is assigned as the half the streamwise span of the FOV at a constant downstream distance marked box A in Fig. 3. As the sphere is towed across the FOV, box A moves with the sphere while the entire box remains within the FOV. The velocity fields inside the box at each snapshot, $u_{x_A}^{t_n}$ are then organized into column vectors:

$$\mathbf{x}_0 = \begin{bmatrix} \mathbf{u}_{x_0}^{t_0} \\ \mathbf{u}_{x_1}^{t_0} \\ \mathbf{u}_{x_2}^{t_0} \\ \vdots \end{bmatrix}, \mathbf{x}_1 = \begin{bmatrix} \mathbf{u}_{x_0}^{t_1} \\ \mathbf{u}_{x_1}^{t_1} \\ \mathbf{u}_{x_2}^{t_1} \\ \vdots \end{bmatrix}, \mathbf{x}_2 = \begin{bmatrix} \mathbf{u}_{x_0}^{t_2} \\ \mathbf{u}_{x_1}^{t_2} \\ \mathbf{u}_{x_2}^{t_2} \\ \vdots \end{bmatrix}, \quad \cdots, \quad (1)$$

where $\mathbf{u}_{x_j}^{t_n}$ represents a column vector of the velocity field at $x/R = x_j$ with respect to the sphere at time t_n, and $\mathbf{x}_n$ is a column vector consisting all $\mathbf{u}_{x_j}^{t_n}$ vectors at $t = n$. This set of vectors is used as an input to DMD in Eq. (5). When the first temporal sequenced set reaches the last available snapshot for a constant streamwise position, the next half of the FOV is available for the next set (marked B in Fig. 3). The number of available snapshots for each set is $m = x_{\text{FOV}}/(2Udt)$.

At a fixed camera FOV with various sphere sizes, box A can be either overly zoomed in to not be able to see the wake structure especially for the horizontal FOV at high Re and low Fr conditions or zoomed out to include multiple evolution stages especially for the small sphere in vertical FOV low Re high Fr conditions. These two scenarios are challenging for DMD to isolate a coherent structure. Therefore, a streamwise box size closest to a constant observation window $x/R = [20, 30]$ among quarter $(0.5x_A)$, half (x_A), and full FOV $(x_A + x_B)$ is selected for the temporal sequence. To obtain the temporal reconfiguration of the full FOV, the FOV from two cameras with parallel viewing angles are appended (subtracting the overlap region) to increase the effective FOV in x. However, since the interest is in the near-wake without developments immediately behind the sphere (i.e. recirculating region), A (as shown in the figure) is not used and DMD is only performed on the temporal sequence following A.

B. Simulation

The stratified wake problem can be set up from the incompressible continuity equation and application of the Boussinesq approximation to the Navier-Stokes momentum equation, where the density variation is only non-negligible when multiplied by $\mathbf{g}$ in the buoyancy

term. The density and pressure fields are decomposed into a background state and a perturbation as $\rho(\mathbf{x},t) = \overline{\rho}(z) + \rho'(\mathbf{x},t)$ and $p(\mathbf{x},t) = \overline{p}(z) + p'(\mathbf{x},t)$ where the background density gradient is in z. After applying the Boussinesq approximation and hydrostatic balance, $(\partial\overline{p}/\partial z = -g\overline{\rho}(z))$, the dimensionless form of the governing equations are

$$\nabla \cdot \mathbf{u} = 0, \tag{2}$$

$$\frac{\partial \mathbf{u}}{\partial t} + \mathbf{u}\cdot\nabla\mathbf{u} = -\nabla p' + \frac{1}{\mathrm{Re}}\cdot\nabla^2\mathbf{u} + \rho'\mathbf{g}, \tag{3}$$

$$\frac{\partial \rho'}{\partial t} + \mathbf{u}\cdot\nabla\rho' = w\cdot\frac{d\overline{\rho}}{dz} + \frac{1}{\mathrm{Pr\ Re}}\cdot\nabla^2\rho', \tag{4}$$

where $\mathbf{u}$ is the velocity field, $t = 1/\mathrm{St}$ is time, $\mathbf{g}$ is the gravitational acceleration in z, w is the vertical velocity in z, and Pr is the Prandtl number. Re and Fr are modified by changing $\tilde{\nu} = 1/\mathrm{Re}$ and $d\overline{\rho}/dz$ with a fixed background flow velocity, $U = 1$, and sphere diameter $D = 1$ fixed at the origin.

The governing equations are implemented in OpenFOAM using a PimpleFOAM solver, which uses a finite volume method with a pressure-velocity coupling algorithm typically used in a transient incompressible CFD. Both temporal and spatial terms are second-order accurate. Boundary conditions are set to zero-gradient conditions on the y-normal and z-normal boundaries to reduce internal wave reflection from the boundaries. To allow for possible breaks in the axisymmetry of the wake, the sphere is oscillated in-line once in three axes each as the initial condition [31].

The unstructured mesh of the computational domain $60D\times16D\times16D$ is distributed where the cell size splits at each grid refinement level closer to the sphere as indicated by the orange box in Fig. 4. The simulation is sampled at $[-1.5, 15]D \times [-2, 2]D \times [-2, 2]D$. The resolution of the coarse mesh used for $\mathrm{Re} = 200, 300, 500$ is about 3 million cells while the fine mesh used for $\mathrm{Re} = 1000$ is about 17 million cells. More details of the numerical setup are in [32].

C. DMD

1. Standard DMD

DMD was applied to the temporal series $\mathbf{x}_k{}_{k=0}^{m}$ of experimental data from Eq. (1) and the simulation, where the fixed sphere reference frame and observation window of $x/R = [20, 30]$ is consistent. Since two 2D centerplanes of the experimental data were sampled independently, DMD is performed independently for the equivalent planes of the simulation (see Section III D). In this project, the SVD-based, standard DMD method described iteschmid:10,rowley:09,chen:12 is used, where the minimized residual is placed on the last snapshot $\mathbf{x}_m$. The algorithm is summarized in the following:

1. Construct snapshots $\{\mathbf{x}_k\}_{k=0}^{m}$ into a data matrix $\mathbf{K}$ and an index-shifted matrix $\mathbf{K_p}$

$$\begin{aligned}\mathbf{K} &:= \begin{bmatrix}\mathbf{x}_0 & \mathbf{x}_1 & \cdots & \mathbf{x}_{m-1}\end{bmatrix}\\ \mathbf{K_p} &:= \begin{bmatrix}\mathbf{x}_1 & \mathbf{x}_2 & \cdots & \mathbf{x}_{m}\end{bmatrix}\end{aligned} \tag{5}$$

2. Compute reduced SVD of $\mathbf{K}$

$$\mathbf{K} = \mathbf{U\Sigma W}^{\mathrm{T}} \tag{6}$$

3. Perform eigendecomposition on a companion matrix $\mathbf{C}$ [27–29]

$$\tilde{\mathbf{C}} := \mathbf{U}^{\mathrm{T}}\mathbf{C}\mathbf{U} = \mathbf{U}^{\mathrm{T}}\mathbf{K_p}\mathbf{W}\mathbf{\Sigma}^{-1} \tag{7}$$

4. Obtain the Ritz vector $\mathbf{V} = \mathbf{UY}$ and Ritz values $\mathbf{\Lambda}$ from

$$\tilde{\mathbf{C}} = \mathbf{Y}\mathbf{\Lambda}\mathbf{Y}^{-1} \tag{8}$$

Ritz values λ_j^k provide the growth rate, $\beta = |\lambda|^{1/\Delta t}R/U$, and Strouhal number (See Eq. (12)) of each DMD mode and the Ritz vector $\mathbf{v}_j$ has the velocity field of each mode.

2. Total DMD for noise-contaminated datasets

In the presence of a low signal-to-noise ratio in the observed data, a total DMD (TDMD or total least-squares DMD), introduced by [33], was used to reach an unbiased result when noise is significant. This method utilizes an augmented matrix of snapshots and time-shifted data in the subspace projection step to prevent asymmetry in the linear fitting process. When noise is minimal in the data as in the simulation, TDMD gives the same result as DMD.

To account for noise from both $\mathbf{K}$ and $\mathbf{K_p}$, an augmented matrix is introduced.

$$\mathbf{Z} := \begin{bmatrix}\mathbf{K}\\ \mathbf{K_p}\end{bmatrix} \tag{9}$$

In this project, we have more spatial resolution in each snapshot than temporal resolution in the number of snapshots, so the DMD problem is under-constrained. As a result, in TDMD, the subspace of $\mathbf{Z}$ may retain traces of noise contamination. Therefore, with $\mathbf{W_r}$, a reduced subspace from the SVD of $\mathbf{Z}$ is projected onto $\mathbf{K}$ and $\mathbf{K_p}$. Then Eq. (7) and (8) is performed where $\mathbf{K}$ and $\mathbf{K_p}$ are now replaced by $\tilde{\mathbf{K}} = \mathbf{KW_r}$ and $\tilde{\mathbf{K}}_\mathbf{p} = \mathbf{K_pW_r}$. Truncation level of $\mathbf{W_r}$ is chosen based on excluding energy content below the noise threshold, $E_{\mathrm{noise}} := \mathrm{RMS}(\tilde{E}(St >$

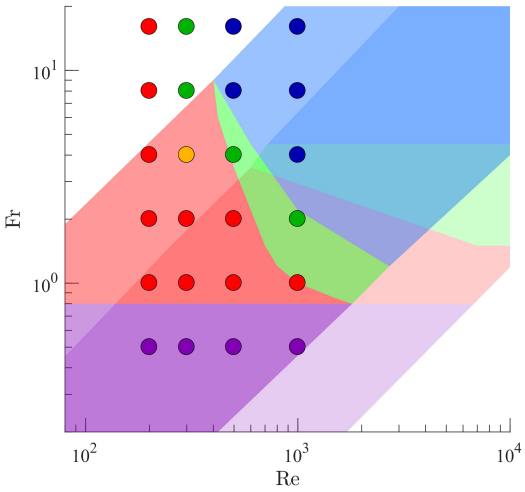

FIG. 5: A regime diagram for stratified sphere wakes. The final result in colored dots combines experiments from CH93 (lighter colors) and LI92 (darker colors) with combined laboratory and numerical experiment. The five identified regimes are labelled and color-coded as: Vortex street (VS, purple), Symmetric non-oscillatory (SN, red), Asymmetric non-oscillatory (AN, yellow), Planar oscillatory (PO, green), and Spiral mode (SP, blue)

1)), which is defined as

$$E_r := 1 - \frac{\Sigma\tilde{E}(\tilde{E} < E_{\text{noise}})}{\Sigma\tilde{E}} \tag{10}$$

where $\tilde{E}$ is normalized modal energy in Eq. (11).

III. RESULTS

A. A combined regime diagram for sphere wakes

Here we propose five regimes for stratified sphere wakes based on the findings of experiments (LI92, CH93) and numerical simulations noted previously [3–7]. The final selection of wake categories is then guided by the current combined experimental and numerical program on the near wakes of spheres in a background stratification [34] which in turn is based partly on computations in [35]. The resulting 5 categories are not as numerous as a superposition of all literature results would yield, and a reconciliation of small differences between LI92 and CH93 is not pursued further, but at these locations in {Re-Fr}, their categorisation into one of the five possible is unambiguous and repeatable.

The combined classification scheme is determined at each of the discrete dots in {Re-Fr} of Fig.5 where both experiments and computations have been run, each on multiple occasions. Samples through these data fields, from both experiment and simulation, will provide the input data for the classification algorithms. Each category is associated with specific physical mechanisms that shape the near wake. Details of variations close to the sphere surface are not taken into account if they do not cause an observable change in pattern that passes into the free wake. We also note the characteristics of any particular DMD mode associated with a physical regime.

The observation window occurs at $x/R = [20, 30]$ and for $\text{Fr} = [0.5, 1, 2, 4, 8, 16]$ the window is equivalent to $Nt = (x/R)/\text{Fr} = [40-60, 20-30, 10-15, 5-7.5, 2.5-3.75, 1.25-1.875]$. If regime boundaries such as 3D-NEQ are fixed in Nt, then the lower Fr data appear firmly in the NEQ regime while the higher Fr data (particularly for $\text{Fr} = 16$) are extracted from a time domain where the adjustment process has only just begun.

B. Distinguishing characteristics

1. *Vortex street (VS)*

When $\text{Fr} \leq 0.7$ the ambient density gradient strongly influences the amplitude of vertical motions over the sphere, and in a central layer fluid particles travel around the obstruction in a horizontal plane where vortex shedding occurs much as in a two-dimensional cylinder wake at low Re in a homogeneous fluid. The wake disturbance is thus primarily characterised by vortex shedding in an equatorial layer, bounded above and below by lee waves that increase in amplitude as $\text{Fr} \to 1$. The quasi-2D vortex wake occurs over all Re examined, $\text{Re} \in [10^2, 10^3]$, but the formation mechanism varies. At lower Re, the shedding is directly from the sphere, passing through an oscillatory phase and then to alternating vortices that appear only further downstream in the wake. It is the signature of the fully-developed wake that is of most interest, rather than details of the origin, so the quasi-2D, 2D oscillating and 2D steady regimes of CH93 are combined into VS here. (The equivalent regimes in LI92 are the non-axisymmetric and symmetric vortex shedding regimes, a nomenclature that focuses on observations close to the sphere surface.) VS is colored purple in the lower Fr row of Fig. 5. The most energetic DMD mode is shown in Fig. 6a. The mode alternates in sign and is v-shaped in the vertical. Other energetic modes include higher harmonics of the vortex street and a mean mode that shows lee waves.

2. *Symmetric, non-oscillatory (SN)*

When Fr is defined on the radius, as it is here, then $\text{Fr} \approx 1$ is when lee waves have their maximum amplitude, $\zeta = D/2$, effectively suppressing vortex shedding and any other oscillatory motions. As detailed in LI92 and CH93, the flow transitions around $\text{Fr} = 1$ lead to intricate separation patterns on the sphere itself. Increasing in x,

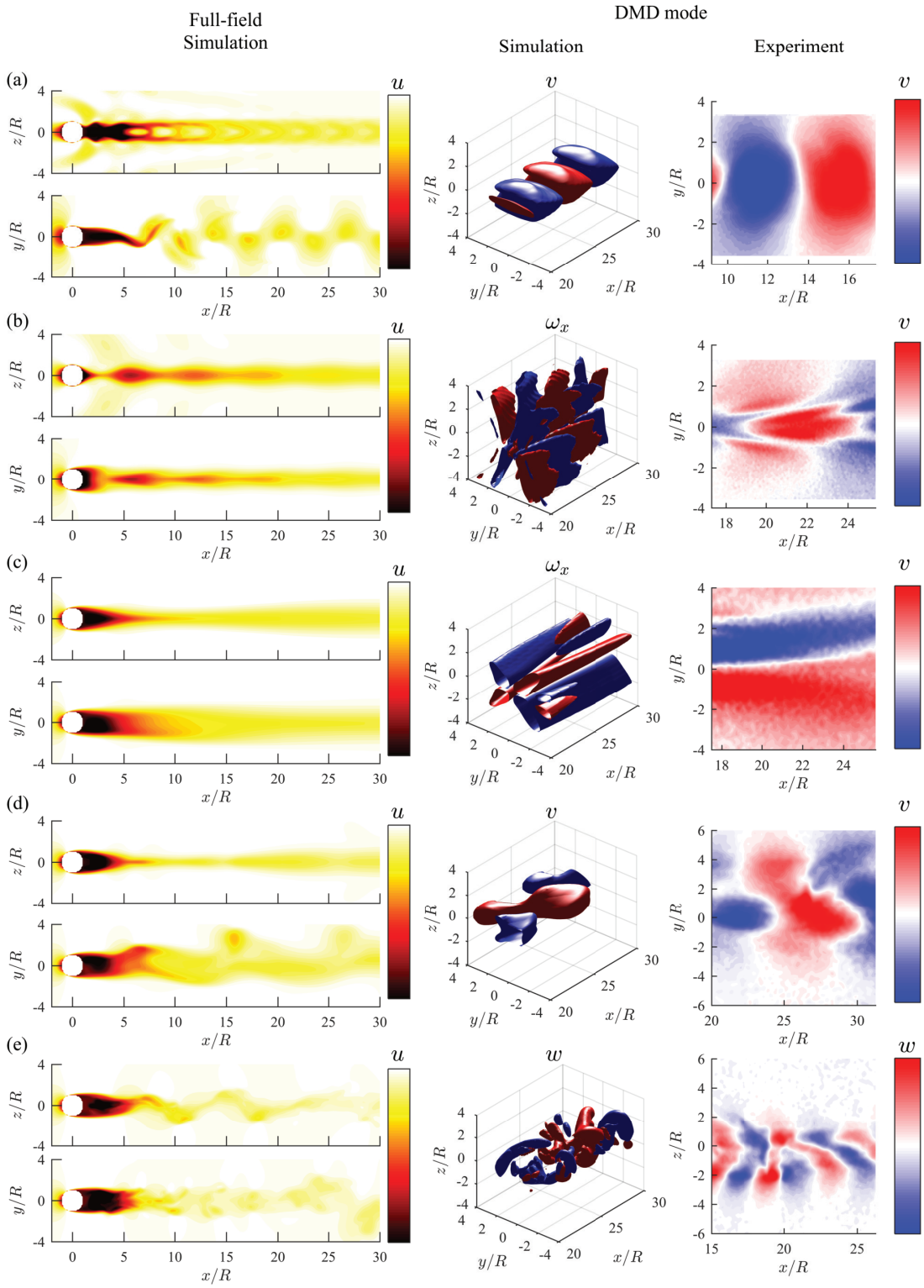

FIG. 6: A snapshot of the flow field u in vertical and horizontal centerplane (left) and a dominant DMD mode of simulation in 3D (middle) and experiment in 2D centerplane (right) illustrating various regimes observed: (a) R10F0.5 Vortex Street (R2F0.5 for the experiment), (b) R5F1 Symmetric Non-oscillatory, (c) R3F4 Asymmetric Non-oscillatory, (d) R3F8 Planar Oscillatory (e) R10F8 Spiral Mode. The isolevel of the middle 3D plot is 30% of the maximum velocity component.

the wake pulses with a wavelength determined by the lee waves. CH93 and [36] show that this wavelength, $\lambda/D = \pi Fr$. These waves are steady in the sphere reference frame, and dominate the near wake, which is therefore symmetric and non-oscillatory. Thus there is a broad range of Fr ≥ 1, Re ≤ 300 where the mean wake disturbances are similar, as shown in red in Fig. 5 The mean DMD mode contains most of the signal energy from the stationary lee waves, and the highest energy oscillatory mode also resembles the mean (Fig. 6b). The wake is symmetric in $xy0$ and in $x0z$ and ω_x most clearly describes its geometry. If data are available from experiment in only one plane, then the v velocity component in the horizontal plane is the most sensitive indicator of the overall geometry.

3. Asymmetric, non-oscillatory (AN)

As Fr increases, the lee wave amplitudes diminish and other modes can appear in the wake. These modes first appear in the horizontal centerplane, and at particular {Re-Fr} the earliest appearance of departures from SN is in an asymmetric mode. In the vertical plane, the wake is symmetric and non-oscillating, similar to SN, but in the $xy0$ plane it is asymmetric about the centerline Fig. 6c. The AN regime is not clearly or separately defined in the literature, but when classification criteria are built from symmetry properties in DMD modes, it is readily distinguishable, even if at only one Re-Fr test case (Re = 300 and Fr = 4, marked yellow in Fig. 5). The AN wake is steady so the most energetic DMD mode is again the mean, but the next most energetic modes share the same pattern, which is measurably asymmetric in y

4. Planar oscillatory (PO)

Generally, as Fr increases above 1, the continued weakening influence of the stratification eventually allows oscillations in both horizontal and vertical planes, becoming fully three-dimensional at higher Fr. The first departure from the SN/AN modes is an oscillatory mode. In the vertical centerplane the internal wavelength is long compared with the body diameter ($\lambda/D \sim Fr$) and contributes to a periodic variation in wake height. In the horizontal plane there are wavy oscillations that are not steady in the sphere reference frame but that have the same wavelength as the vertical variations, which are. This mode is observed at the boundary in Re-Fr space between AN/SN and the spiral mode which is fully three-dimensional. In this regime, vortex shedding and roll-up are possible in the horizontal plane, but all vertical motions are subsumed into the dominant lee wave mode. The boundary marking this mode is approximately on fixed Fr Re^{-1}, as originally noted in CH93, and PO modes are labelled green in Fig. 5. The combined vortex and wave motions lead to a most energetic DMD mode as an angled structure alternating in y, as shown in Fig. 6d.

5. Spiral mode (SP)

As both Re and Fr increase, the two major instability modes of the neutral wake are recovered – the Kelvin-Helmholtz and spiral modes. The Fr at which K-H modes appear decreases as Re increases, and at sufficiently high {Re-Fr} the K-H shear-layer instabilities are found alongside the truly three-dimensional spiral mode. SP is marked not just by the long spiral wavelength but also by the appearance and persistence of small-scale turbulence. SP appears in blue at the top right corner of Fig. 5. SP is shown in Fig. 6e. It is the increased activity in the vertical that distinguished this regime from others, and the DMD modes in the vertical velocity component in the vertical $x0z$ plane can be used to uniquely identify it. The spiral wavelength is about $6D$ in streamwise extent so the DMD modes from simulation and experiment may not contain a full cycle, depending on the window length in x. Since this regime characterises the move to higher Re and Fr, future work will focus on discriminating patterns inside this regime.

C. Automated 3D wake classification

The distinguishing characteristics of the five regimes introduced in Section III B are accentuated when projected onto DMD modes that act like a dynamic shape or structure filter. Then algorithms can be designed to interrogate these modes for classification into the corresponding regimes. DMD is computed on a $\mathbf{K}$ matrix, a temporally reconfigured flow data stream, based on Section II A 1 producing a total number of modes equal to the number of snapshots. The modes are then sorted based on energy as

$$\tilde{E}_j := \frac{\sqrt{m+1}\,|\lambda|_j^m \|\mathbf{v}\|_2}{\|[\mathbf{K}\ \mathbf{x}_m]\|_\mathrm{F}}, \tag{11}$$

where the modal energy $\|\mathbf{v}\|_2$ is scaled to $|\lambda|^m\|\mathbf{v}\|_2$, a contribution of the j^{th} mode in the reconstruction of the last snapshot, x_m, normalized by the rms of the data norm, $\|[\mathbf{K}\ \mathbf{x}_m]\|_\mathrm{F}/\sqrt{m+1}$. The Strouhal number of each j^{th} mode is then

$$\mathrm{St}_j := \frac{\omega_j R}{2\pi U} = \frac{\arg(\lambda_j)\,R}{2\pi \Delta t\, U}, \tag{12}$$

where $\arg(\lambda)/\Delta t$ is equivalent to a phase angular velocity and Δt is the time interval between two consecutive snapshots. The St range is limited by $\max(\arg(\lambda)) = \pi$, for a maximum $\mathrm{St}_{\max} = R/(2\Delta t U)$. In the simulations, $\mathrm{St}_{\max} = 0.5$ for low Re and $\mathrm{St}_{\max} = 1.25$ for Re = 1000; for the experiments, $\mathrm{St}_{\max}$ is generally much higher as smaller Δt are required for the PIV estimates.

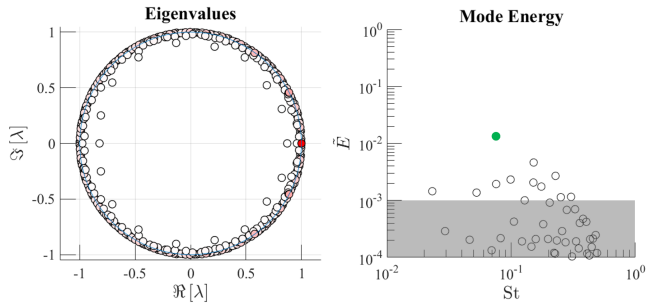

(a) Simulation

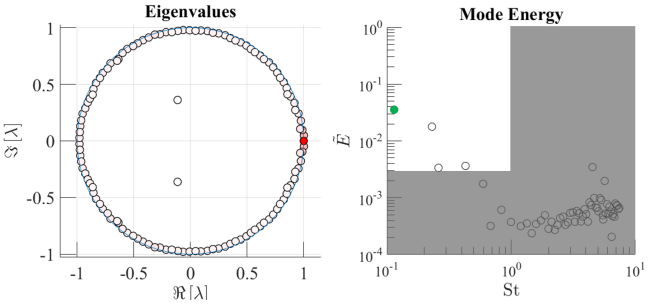

(b) Experiment

FIG. 7: The plots on the left show the real and imaginary parts of λ, and on the right $\tilde{E}(\mathrm{St})$ is shown for each mode of the case $\mathrm{Re} = 500$ and $\mathrm{Fr} = 4$. The dark red corresponds to the mean mode. The green dot is the most dominant mode selected to be evaluated in Fig. 8. The grey area is considered noise, set below $\tilde{E}$ threshold and above St threshold.

1. *Mode selection criteria*

As the stratified wakes evolve, smaller-scale vortices merge into large-scale pancake eddies. Low St modes associated with these objects then contain most energy while high St modes associated with small scales, noise, or high-order harmonics have much lower energy, as shown in the frequency spectra of DMD modes in Fig. 7. When DMD is computed from a full field, the highest energetic mode resembles the mean flow with $\mathrm{St} \simeq 0$ (marked in red at $\lambda \simeq 1$ in Ritz value Fig. 7 and omitted in the plots of $\tilde{E}(St)$). Most modes are temporally neutrally stable as they are near the unit circle.

Minor modes are filtered out by setting $\tilde{E}$ and St thresholds. The combined effects of viscosity and/or an energy cascade mean that most energy in the wakes resides in low-St (or even mean) modes. A robust classifier ought to depend primarily on these modes, so thresholds on $\tilde{E}$ and on St are imposed. In simulations a simple threshold of $\tilde{E} > 10^{-3}$ was found, empirically, to reduce the number considered to 10 or fewer. In the experiment, non-physical small-scale noise (ultimately attributable to PIV errors) shows an increase in energy for $St \geq 1$ and this limit is also applied. These somewhat arbitrarily selected constant thresholds are supported to some extent by their continued utility following changes in the algorithm (e.g. TDMD, explained more in detail in Section III D 3), and the fact that selections based on the highest ranked modes only are not sensitive to the existence of large numbers of sub-threshold modes.

Consequently, the oscillatory (or non-zero frequency) mode with the highest $\tilde{E}$ (marked in green in Fig. 7) is selected for further interrogation. If there are no oscillatory modes in the viable mode selection pool (following threshold), the flow is in the non-oscillatory regime, and this mean mode is selected for further evaluation in the non-oscillatory branch of the classifier. In all cases, the mode in question is then classified into a regime described in Section III B, based on criteria that depend on the symmetry and energy distribution along x about $y = 0$ or $z = 0$. This classification procedure is summarized in the flowchart in Fig. 8, and the sequence of decision points is described below.

2. *Non-oscillatory regimes: Symmetric or Asymmetric*

The two non-oscillatory regimes are distinguished based on the symmetry of the energy distribution of the mean mode about $y = 0$. The degree of symmetry is determined through the difference norm of the streamwise vorticity ω_x in $\pm y$ in x and z,

$$\Delta|\omega_x| := \frac{|\|\omega_x(-y)\| - \|\omega_x(+y)\||}{\|\omega_x\|}. \tag{13}$$

When $\Delta|\omega_x| \leq 20\%$, the flow is in the symmetric, non-oscillatory regime (SN) and otherwise it is in the asymmetric non-oscillatory (AN) regime. (Full asymmetry would yield $\Delta|\omega_x|_{\max} = 1$.)

3. *Oscillatory regimes: Planar motion or Spiral Mode*

In the oscillatory branch on the right side of the decision tree in Fig. 8, the symmetry of $v(x, z)$ in the z direction readily distinguishes the spiral mode from regimes where flow is confined close to the horizontal centerplane. In the vertical direction of the planar motion, symmetric pulsation in the PO regime and the V-shaped structure in VS are both spatially invariant with respect to the sphere, and symmetric about the horizontal centerplane. By contrast, the spiral mode has spatial variation in z, asymmetric about $z = 0$. The symmetry measure is

$$\Delta v_{\pm z} := \frac{\|v_{-z} - v_{+z}\|}{\|v\|}, \tag{14}$$

where v_{+z} is the lateral velocity of the upper half of the field, $v(x, 0, +z)$, about the centerplane of the wake. Though the symmetry can also be estimated from the vertical velocity w, the magnitude of w is relatively small for the planar motion branch so that $\Delta w_{\pm z}$ would be sen-

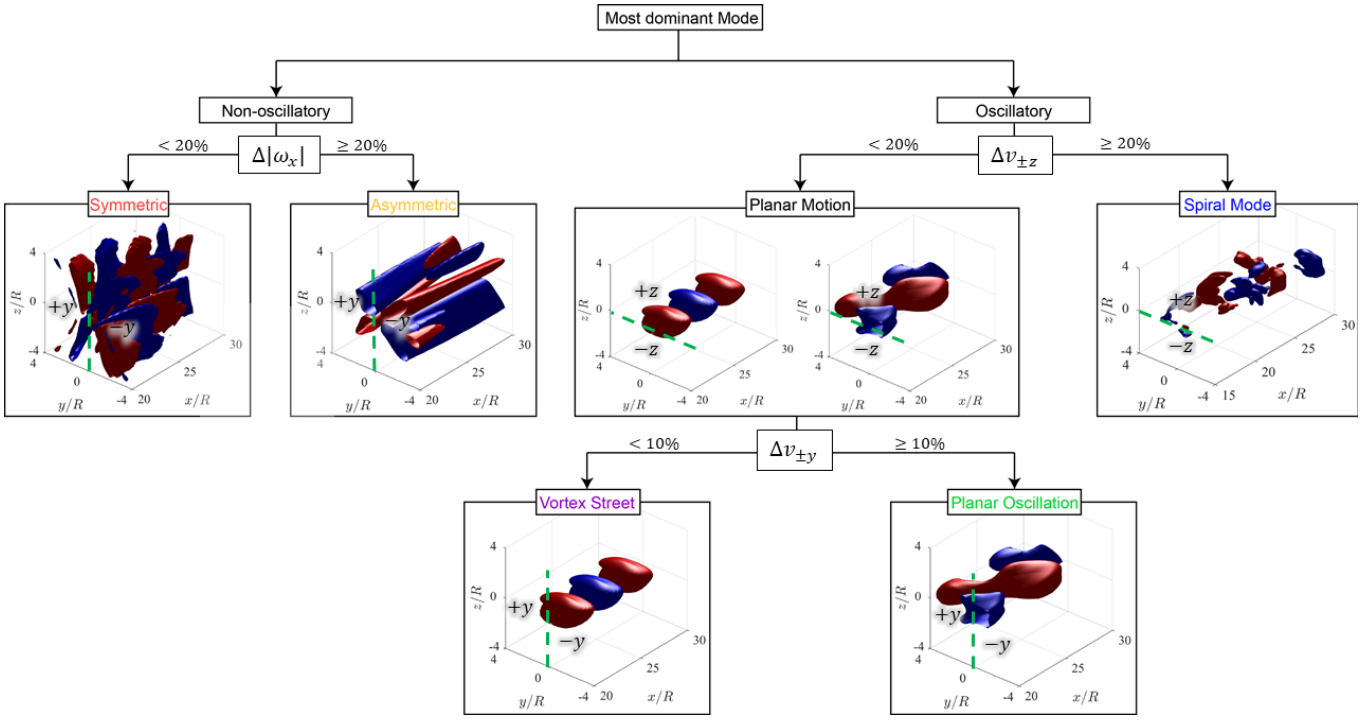

FIG. 8: A flow chart of the wake classifier with 3D DMD input. The selected DMD mode from Section III C 1 is sorted into five regimes in the non-oscillatory branch (left) and oscillatory branch (right) based on the symmetry of the cross-stream velocities in that mode.

sitive to noise. In contrast to interrogating the symmetry of the energy distribution in Eq. (13) for the non-oscillatory branch, the oscillatory branch constructs a point-by-point difference mirroring the top and bottom half of the field. For $\Delta v_{\pm z,\min} = 0 = 0\%$ the DMD mode is perfectly symmetric about the horizontal plane and when $\Delta v_{\pm z,\max} = \sqrt{2} = 100\%$ the upper and lower half of the field are equal and opposite. A symmetry level tolerance of 20% is set by taking the average of $\Delta v_{\pm z}$ from all available sets in each regime decision box, similar to a cross-validation method that allows small asymmetries from instabilities in the spiral mode. When $\Delta v_{\pm z}$ is less than 20%, the mode is either in VS or PO regime.

4. *Planar motion: Vortex Street or Planar Oscillation*

In the Planar motion branch, a dominant mode in VS has alternating signed structures aligned along the wake centerline, with symmetry in both y and z. Since symmetry in z was satisfied earlier in the decision tree, symmetry in y now distinguishes VS from PO. The symmetry between the left and right half of the v about $y = 0$ can be calculated in the same way as Eq. (14) as a function of $v_{\pm y}$. When $\Delta v_{\pm y}$ is greater than 10%, the mode is considered asymmetric in y, and hence in the planar oscillation regime. The coherence of the quasi-2D vortex street that occurs in the VS regime allows the symmetry tolerance in y to be tighter ($\Delta v_{\pm y} = 10\%$) than in z ($\Delta v_{\pm z} = 20\%$). Since the stratified wake evolves, albeit slowly, in the streamwise direction, all criteria are evaluated based on the local cross-stream information.

5. *Success rate of the classifier with 3D numerical DMD input*

There are 24 {Re-Fr} points for the classifier and in each one, the correct category is known (as VS, SN, AN, PO, SP). The accuracy can then be determined and is synonymous with the success rate. The success rate of the classifier described in Fig. 8 is illustrated in Fig. 9 for each Re − Fr pair. In the numerical study, the full 3D flow field is available, while only two centerplanes (horizontal and vertical) are available from the experiment. The test samples were collected from equally splitting one continuous simulation into 10 (or multiple) sets at different time instances. (The total number of sets was determined based on ensuring the independence of the number of snapshots in a set to minimize aliasing error). The color in the pie chart for each case in the Re − Fr parameter space shows the classification distribution. When the pie chart is filled with one uniform color, the classifier has 100% accuracy.

Most cases have a 100% success rate. The 6 cases that

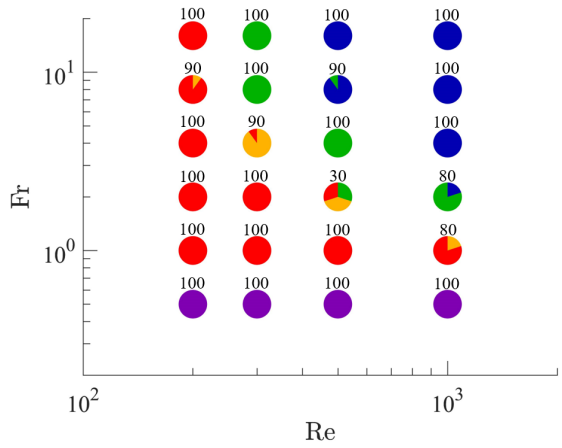

FIG. 9: Success rate of a classifier with 3D numerical DMD input. The pie chart shows the classification type in color. The number above each filled circle is the the percent accuracy of the majority outcome.

do not live close to regime borders. The worst case at $\mathrm{Re} = 500, \mathrm{Fr} = 2$ with only 30% success rate, when misclassified was always classified in one of three neighboring regimes (SN, AN, and PO), caused by occasional small oscillation in the lateral direction. The small oscillations come from slight unsteadiness in the recirculation zone and the resulting unsteady DMD modes led the classifier to the oscillatory branch in Fig. 8, even though the modal energy was very close to the energy threshold, $\tilde{E} > 10^{-3}$, in Section III C 1.

D. Wake classification of spatially reduced information

The automated classifier relies on having 3D information of the wake in multiple consecutive snapshots. However, obtaining high dimensional data from an imagined large-scale stratified wake, and even in a laboratory experiment is challenging. In this section, limitations and possible improvements of spatially reduced input information will be examined.

The information available from the laboratory experiment is in two, 2D centerplane (horizontal and vertical) cuts, where each plane is acquired independently. To compare the classification success of DMD modes restricted to one plane, the mode selection is forced towards modes that are available from that plane. For example, in the presence of strong stratification, the most energetic 3D mode(s) may not be obvious when information is restricted to the vertical direction. To guide the classifier to select a similar mode in both planes, the selected mode in the vertical plane is forced to the mode with St_w closest to St_v, the St of the dominant mode from the horizontal plane. From these two matched $\mathrm{St}_{w,v}$, the mode that is in the direction of the plane of interest was used

The flowchart was modified so the direction of symmetry remains the same but the velocity information is confined to the same plane, as illustrated in Fig. 10. Thus, ω_x in Section III C 2 is replaced by v to determine the symmetry in y; v in Section III C 3 is replaced by w to determine the symmetry in z to distinguish SP from planar motion based on flow variation in the vertical direction only; and v symmetry in y in Section III C 4 is unchanged as the velocity and line of symmetry are already in the same direction.

1. *Success rate of the classifier with 2D numerical DMD input*

To understand the performance of the classifier with limited spatial information compared with the 3D numerical input and to keep similar constraints as the experiment, the same simulation data set in Section II B is modified to replicate the spatial limitation of two independent 2D planes from the experiment. The results are summarized in Fig. 11. While most cases in the VS, PO and SN had a high success rate, SP cases bordering the PO regime had a measurably lower success rate (though above 50%). Since SP is the only regime among the five that has flow variation in the vertical direction, the (comparative) failure could have come from the procedure of choosing the dominant mode in the vertical direction based on $\mathrm{St}_w \simeq \mathrm{St}_v$. Note however that the lower success rate of VS does not come from misclassification to a neighboring regime in {Re-Fr}.

2. *Success rate of the classifier with 2D experimental DMD input*

The same criteria from Fig. 10 were applied to the two 2D planes of experimental results, and results are shown in Fig. 12. The more strict the classification criteria (e.g. $\tilde{E}$ threshold, symmetry requirement), the more the errors increase. In particular, many non-oscillating regimes were incorrectly classified into the oscillatory branch for zero success rate. As noted in Section III C 1, the successful classification of non-oscillatory regimes relies heavily on the energy threshold $\tilde{E}_{\max}(\mathrm{St} > 1)$. When the real wake flow is steady with respect to the sphere, the small amplitude time-varying input components, which are either noise or small variations in mean wake position (in y and/or z), come to dominate the DMD modes.

The influence of small-scale noise typical of experimental conditions can be reduced by performing DMD on an appended vector of the measurement and a time-shifted value, $[\mathbf{x}_k^{\mathrm{T}} \mathbf{x}_{k+1}^{\mathrm{T}}]^{\mathrm{T}}$, known as TDMD (see Eq. (9) in Section II C 2), when the data matrices $\mathbf{K}$ and $\mathbf{K_p}$ become linearly consistent [33, 37]. Improvement of the classifier using TDMD is discussed in the following Section III D 3.

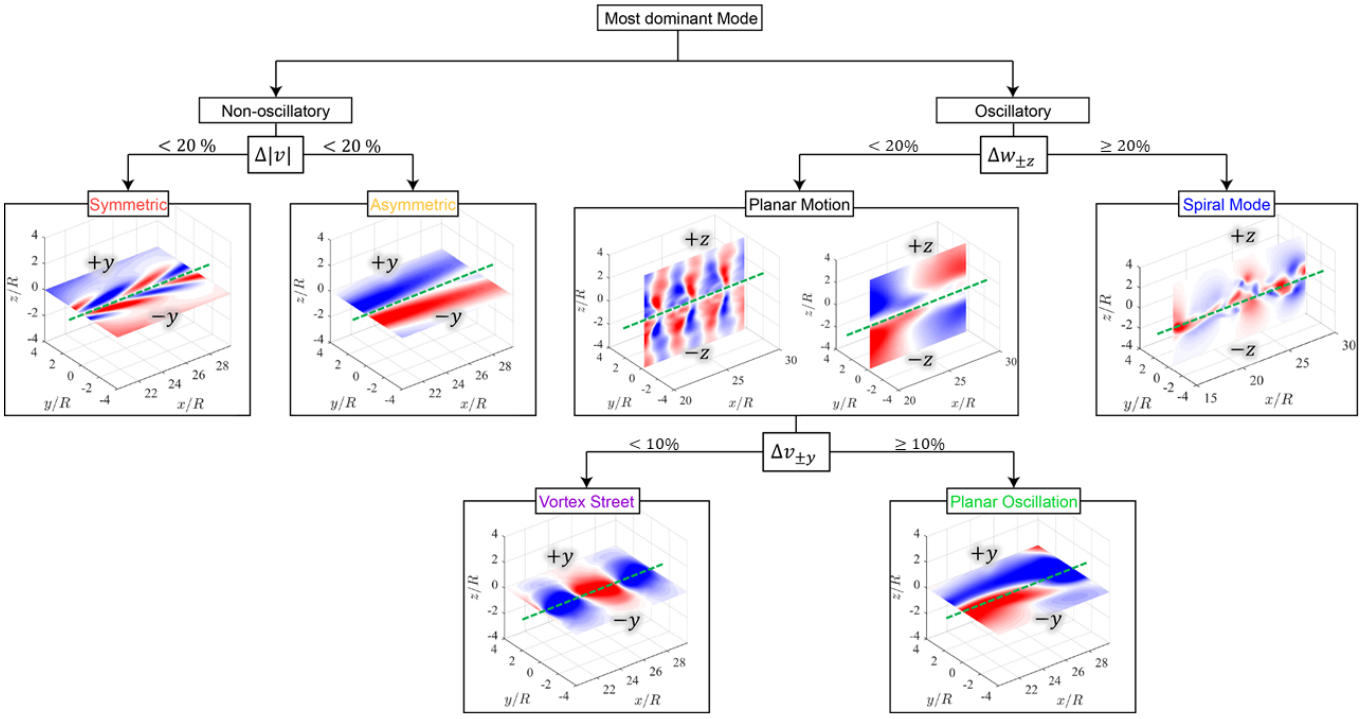

FIG. 10: A flow chart of the wake classifier with two, 2D-centerplane flow fields as input. Two dominant DMD modes of each centerplane are evaluated where the mode for the vertical centerplane is selected based on St_w closest to St_v. The non-oscillatory branch uses the mode from the horizontal centerplane, while the oscillatory branch uses the vertical centerplane for the first step, and horizontal centerplane for the second step. Green dotted line represents the wake centerline.

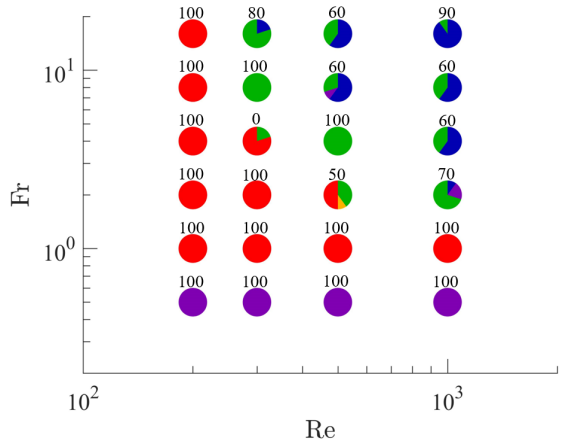

FIG. 11: Classifier success rate with 2D numerical DMD input.

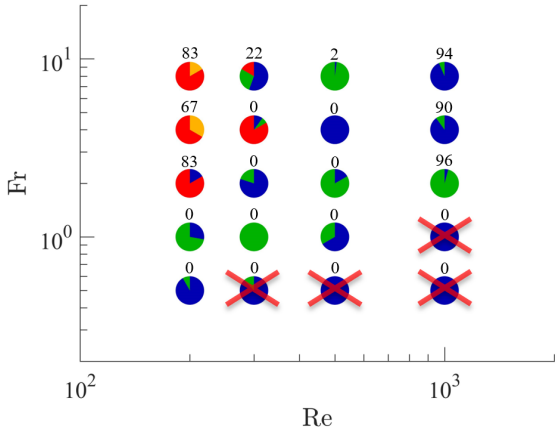

FIG. 12: Classifier success rate with 2D experimental DMD input. Cases with Red X have wake lengthscales larger than the FOV for regimes to be distinguishable.

In strongly stratified wakes, the body-fixed lee wave forces much of the fluid mechanical information to be steady in the sphere reference frame. Experiments conducted in the laboratory reference frame are converted through a constant shift to this reference frame but then if the computed shift is not exactly correct, there are small residual apparently unsteady motions which, in a DMD analysis will lead to 'shadows' of the mean mode in the most energetic oscillatory modes.

Finally, when the wake lengthscales in any direction are comparable to or larger than the field of view, the algorithm yields results (marked off in a red X in Fig. 12) that are influenced by the spatial truncation. Therefore, only cases with window width in y are bigger than $3R$ are evaluated.

3. TDMD based classifier for noise-contaminated input

Following the application of TDMD in Section II C 2, the dominant TDMD mode of an example non-oscillating case is compared against the dominant standard DMD mode in Fig. 13. The main struggle of the DMD-based classifier lies in dealing with a planar view of the flow field in which the dominant oscillatory mode is not present. Then modes triggered by noise are erroneously selected as dominant modes (e.g. SN, AN regimes, and vertical centerplane of VS and PO regimes). This is shown in a sample SN regime case in the horizontal centerplane at Re = 300 and Fr = 2 in Fig. 13a where noisy energetic modes are not filtered out by the energy threshold, $\tilde{E}_{\text{noise}}$, to yield a success rate of 0% in Fig. 12. The same flow field computed on TDMD is shown in Fig. 13b where the truncation level of $r = 97$ from $m = 276$ total snapshots was used based on $E_r = 91.6\%$ from Eq. (10). Although most DMD modes lie on the unit circle, appearing neutrally stable, the TDMD modes are concentrated near $\lambda = 1$ (i.e. mean mode) and otherwise lie inside the unit circle. This shows that non-mean modes are damped out, as is physically realistic in a decaying flow. The energy of higher modes for St > 1 is significantly reduced. The most energetic DMD mode with St $= 0.02$ showed a flow structure similar to the mean mode (but contaminated with noise), which no longer appeared in the TDMD spectra, while the dominant sDMD mode at St $= 0.05$ was quite different from the mean mode. The shift in dominant modes from DMD to TDMD shows that the noise-related small variations in the mean mode ($\tilde{E} \sim 1$) can appear as an energetic oscillatory mode. Although these TDMD modes once again place the flow (incorrectly) into the PO regime, the energy of dominant oscillatory modes is significantly reduced and the mode shape is more coherent (Fig. 13b). This example case in SN is the toughest condition to obtain a clean result, as TDMD is applied to a flow field that varies little in x. Data with physically-correct spatial variation can be expected to significantly improve a TDMD-based classifier.

IV. DISCUSSION

The main objectives of this study were to investigate the feasibility of a DMD-based flow classifier for stratified wakes. The known qualitatively different flow regimes at moderate Fr and Re provide a convenient testbed for such an effort. Given these obvious regime differences it is perhaps unsurprising that initial success rates were very high, as they are for a well-trained fluid mechanician. If this example problem set seems too easy, then at least success can be claimed so as to encourage further exploration in more demanding cases.

Looking outward to more realistic applications, it will never be the case that we have full 3D, time-resolved information on an unknown flow. Following the first successes, a start in systematic reduction of the input data dimension was tested and indeed success rates dropped, but not to zero. The failures do not lead inevitably to the conclusion that the classification basis is flawed (although it might be) and refinements in the DMD computation that eliminate the effect of small-scale noise were successful. The classifier failed in a number of cases that could be unique to the low {Re-Fr} domain, and the problem of small fluctuations superimposed on a dominant mean mode is much more challenging at low Fr when body-fixed lee waves enforce the mean mode dominance. Flows typically found in geophysical applications may occur in a strongly stratified turbulence regime, where Fr is low even though Re remains high. Though this domain is difficult to access in experiment, the expected shear instabilities would generate signals that are readily distinguished from noise.

It is likely that further extensions and tests of this DMD-based classifier will push to domains of higher Fr and higher Re. There the influence of mean modes will be negligible, and it is less clear how the classifier categories will be compiled and extracted. If these categories cannot be defined *a priori* then the entire approach of designer-categories may be impractical. Instead, a more robust and extensible method should be based on some kind of data-driven sorting and categorisation. Such classifiers and learning algorithms from multilayer neural network architectures (deep-learning methods) are well-known and we suggest that such a program could be implemented, first using the known and simple cases described here, and then extrapolating to higher {Re-Fr}. The exploration of classifier space could be purely data-driven, or constrained on a reduced order physical basis. We remark that success (or failure) rates at higher {Re-Fr} in a data-driven program may be completely independent of any pattern of weight matrices learned at lower {Re-Fr}.

ACKNOWLEDGMENTS

This work was supported by ONR contracts N00014-15-1-2506 and N00014-20-1-2584 to whom we are most grateful. We are also indebted to Xinjiang Xiang and Trystan Madison who started this program and implemented and ran the numerical codes whose results are used here. This effort was, in turn, greatly assisted by Dr Kevin Chen while he performed post-doctoral studies in our laboratory.

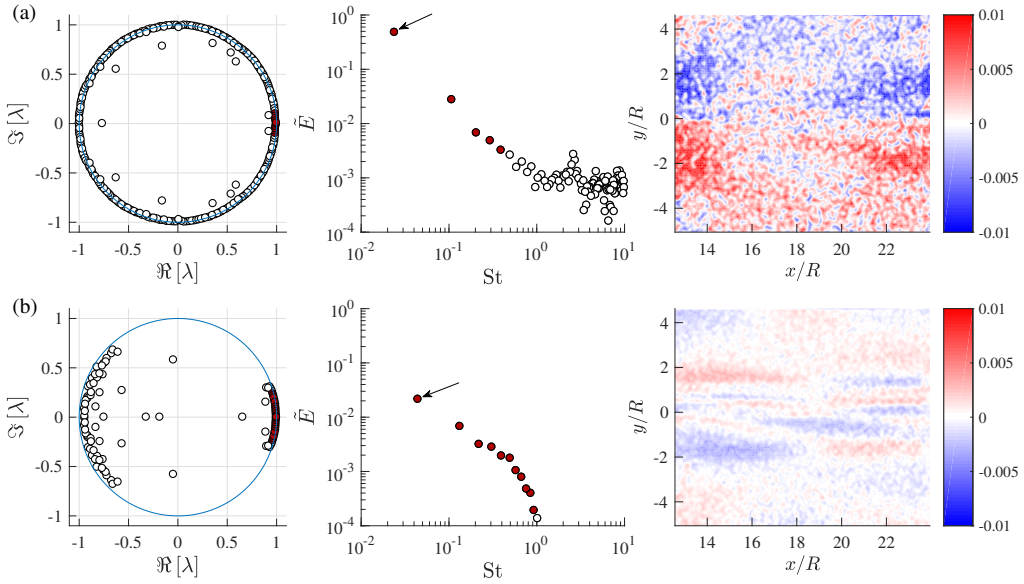

FIG. 13: Ritz values λ (left), $\tilde{E}$ versus St (center), $v(x, y, z = 0)$ of a dominant oscillatory mode (indicated by an arrow) for the $\mathrm{Re} = 300$, $\mathrm{Fr} = 2$ case computed from (a) standard DMD ($E_r = 100\%$ of $\tilde{E}$) and (b) TDMD ($E_r = 91.6\%$). Modes colored in red are energetic modes selected from Section III C 1

[1] Q. Lin, W. R. Lindberg, D. L. Boyer, and H. J. S. Fernando, Stratified flow past a sphere, J. Fluid Mech. **240**, 315 (1992).

[2] J.-M. Chomaz, P. Bonetton, and E. J. Hopfinger, The structure of the near wake of a sphere moving horizontally in a stratified fluid, J. Fluid Mech. **254**, 1 (1993).

[3] H. Hanazaki, A numerical study of three-dimensional stratified flow past a sphere, J. Fluid Mech. **192**, 393 (1988).

[4] T. S. Orr, J. A. Domaradzki, G. R. Spedding, and G. S. Constantinescu, Numerical simulations of the near wake of a sphere moving in a steady, horizontal motion through a linearly stratified fluid at Re = 1000, Phys. Fluids **27**, 035113 (2015).

[5] A. Pal, S. Sarkar, A. Posa, and E. Balaras, Regeneration of turbulent fluctuations in low-Froude-number flow over a sphere at a Reynolds number of 3700, J. Fluid Mech. **804**, R2 (2016).

[6] K. Chongsiripinyo, A. Pal, and S. Sarkar, On the vortex dynamics of flow past a sphere in Re = 3700 in a uniformly stratified fluid, Phys. Fluids **29**, 020703 (2017).

[7] A. Pal, S. Sarkar, A. Posa, and E. Balaras, Direct numerical simulation of stratified flow past a sphere at subcritical Reynolds number of 3700 and moderate Froude number, Journal of Fluid Mechanics **826**, 5 (2017).

[8] G. R. Spedding, F. K. Browand, and A. M. Fincham, Turbulence, similarity scaling and vortex geometry in the wake of a towed sphere in a stably stratified fluid, J. Fluid Mech. **314**, 53 (1996).

[9] G. R. Spedding, The evolution of initially turbulent bluff-body wakes at high internal Froude number, J. Fluid Mech. **337**, 283 (1997).

[10] P. Meunier and G. R. Spedding, A loss of memory in stratified momentum wakes, Phys. Fluids **16**, 298 (2004).

[11] M. J. Gourlay, S. C. Arendt, D. C. Fritts, and J. Werne, Numerical modeling of initially turbulent wakes with net momentum, Phys. Fluids **13**, 3783 (2001).

[12] D. G. Dommermuth, J. W. Rottman, G. E. Innis, and E. A. Novikov, Numerical simulation of the wake of a towed sphere in a weakly stratified fluid, J. Fluid Mech. **473**, 83 (2002).

[13] K. A. Brucker and Sarkar, A comparative study of self-propelled and towed wakes in a stratified fluid, J. Fluid Mech. **652**, 373 (2010).

[14] P. J. Diamessis, G. R. Spedding, and J. A. Domaradzki, Similarity scaling and vorticity structure in high-Reynolds-number stably stratified turbulent wakes, J. Fluid Mech. **671**, 52 (2011).

[15] R. Pasquetti, Temporal/spatial simulation of the stratified far wake of a sphere, Comput. Fluids **40**, 179 (2011).

[16] G. Brethouwer, P. Billant, E. Lindborg, and J. M. Chomaz, Scaling analysis and simulation of strongly stratified turbulent flows, J. Fluid Mech. **585**, 343 (2007).

[17] S. de Bruyn Kops and J. Riley, The effects of stable stratifiecation on the decay of initially isotropic homogenous tubulence, Journal of Fluid Mechanics **860**, 787 (2019).

[18] Q. Zhou and P. J. Diamessis, Large-scale characteristics of stratified wake turbulence at varying Reynolds number, Physical Review Fluids **4**, 084802 (2019).

[19] P. M. Bevilaqua and P. S. Lykoudis, Turbulence memory in self-preserving wakes, J. Fluid Mech. **89**, 589 (1978).

[20] W. K. George, The self-preservation of turbulent flows and its relation to initial conditions and coherent structures, in *Advances in Turbulence*, edited by W. K. George and R. E. A. Arndt (Hemisphere, NY, 1989) pp. 39–73.

[21] P. B. V. Johansson, W. K. George, and M. J. Gourlay,

Equilibrium similarity, effects of initial conditions and local Reynolds number on the axisymmetric wake, Phys. Fluids **15**, 603 (2003).
[22] J. A. Redford, I. P. Castro, and G. N. Coleman, On the universality of turbulent axisymmetric wakes, Journal of fluid mechanics **710**, 419 (2012).
[23] A. A. Townsend, *The Structure of Turbulent Shear fFow*, 2nd ed. (Cambridge University Press, Cambridge, UK, 1976).
[24] G. R. Spedding, Wake signature detection, Ann. Rev. Fluid Mech. **46**, 273 (2014).
[25] P. J. Diamessis, R. Gurka, and A. Liberzon, Spatial characterization of vortical structures and internal waves in a stratified turbulent wake using proper orthogonal decomposition, Phys. Fluids **22**, 086601 (2010).
[26] X. Xiang, K. K. Chen, and G. R. Spedding, Dynamic mode decomposition for estimating vortices and lee waves in a stratified wake, Exp. Fluids **58**, 56 (2017).
[27] P. J. Schmid, Dynamic mode decomposition of numerical and experimental data, J. Fluid Mech. **656**, 5 (2010).
[28] C. W. Rowley, I. Mezić, S. Bagheri, P. Schlatter, and D. S. Henningson, Spectral analysis of nonlinear flows, J. Fluid Mech. **641**, 115 (2009).
[29] K. K. Chen, J. H. Tu, and C. W. Rowley, Variants of dynamic mode decomposition: boundary condition, Koopman, and Fourier analyses, J. Nonlin. Sci. **22**, 887 (2012).
[30] X. Xiang, T. J. Madison, P. Sellappan, and G. R. Spedding, The turbulent wake of a towed grid in a stratified fluid, J. Fluid Mech. **775**, 149 (2015).
[31] S. Lee, A numerical study of the unsteady wake behind a sphere in a uniform flow at moderate reynolds numbers, Comput. Fluids **29**, 639 (2000).
[32] X. Xiang, K. K. Chen, and G. R. Spedding, Experiments and simulations of low re sphere wakes with and without stratification, Int. Sym. Stratified flows (2016).
[33] M. S. Hemati, C. W. Rowley, E. A. Deem, and L. N. Cattafesta, De-biasing the dynamic mode decomposition for applied Koopman spectral analysis of noisy datasets, Phys. Fluids **26**, 111701 (2014).
[34] T. Madison, X. Xiang, and G. R. Spedding, The near wake of a sphere in a background density gradient, Phys. Rev. Fluids (2021), in prep.
[35] X. Xiang, *Laboratory and numerical experiments on the near wake of a moving body in a stratified fluid*, Ph.D. thesis (2017).
[36] P. Meunier, S. e Dizes, L. G. Redekopp, and G. R. Spedding, Internal waves generated by a stratified wake: experiment and theory, J. Fluid Mech. **846**, 752 (2018).
[37] J. H. Tu, C. W. Rowley, D. M. Luchtenburg, S. L. Brunton, and J. N. Kutz, On dynamic mode decomposition: Theory and applications, J. Comput. Dyn. **1**, 391 (2014).